

## RESEARCH LETTER

10.1002/2017GL074620

## Key Points:

- Coseismic surface displacement from DInSAR aligns with a distinct NW striking NE dipping magnetic lineament in the basement
- NW striking NE dipping magnetic lineament represents a thrust splay within the Precambrian Limpopo-Shashe orogenic belt
- The earthquake focal mechanism is consistent with extensional reactivation of a crustal-scale Precambrian thrust splay

## Supporting Information:

- Supporting Information S1
- Table S1
- Table S2

## Correspondence to:

E. A. Atekwana,  
atekwana@udel.edu

## Citation:

Kolawole, F., E. A. Atekwana, S. Malloy, D. S. Stamps, R. Grandin, M. G. Abdelsalam, K. Leseane, and E. M. Shemang (2017), Aeromagnetic, gravity, and Differential Interferometric Synthetic Aperture Radar analyses reveal the causative fault of the 3 April 2017  $M_w$  6.5 Moiyabana, Botswana, earthquake, *Geophys. Res. Lett.*, **44**, 8837–8846, doi:10.1002/2017GL074620.

Received 20 JUN 2017

Accepted 24 AUG 2017

Accepted article online 29 AUG 2017

Published online 9 SEP 2017

## Aeromagnetic, gravity, and Differential Interferometric Synthetic Aperture Radar analyses reveal the causative fault of the 3 April 2017 $M_w$ 6.5 Moiyabana, Botswana, earthquake

F. Kolawole<sup>1,2</sup> , E. A. Atekwana<sup>1,3</sup> , S. Malloy<sup>4</sup> , D. S. Stamps<sup>4</sup> , R. Grandin<sup>5</sup> , M. G. Abdelsalam<sup>1</sup> , K. Leseane<sup>6</sup> , and E. M. Shemang<sup>7</sup> 

<sup>1</sup>Oklahoma State University, Stillwater, Oklahoma, USA, <sup>2</sup>Now at ConocoPhillips School of Earth and Energy, University of Oklahoma, Norman, Oklahoma, USA, <sup>3</sup>Now at Department of Geological Sciences, College of Earth, Ocean, and Environment, University of Delaware, Newark, Delaware, USA, <sup>4</sup>Department of Geosciences, Virginia Tech, Blacksburg, Virginia, USA, <sup>5</sup>Université Paris Diderot, Paris, France, <sup>6</sup>School of Earth Atmosphere and Environment, Monash University, Melbourne, Victoria, Australia, <sup>7</sup>Botswana International University of Science and Technology, Palapye, Botswana

**Abstract** On 3 April 2017, a  $M_w$  6.5 earthquake struck Moiyabana, Botswana, nucleating at >20 km focal depth within the Paleoproterozoic Limpopo-Shashe orogenic belt separating the Archean Zimbabwe and Kaapvaal Cratons. We investigate the lithospheric structures associated with this earthquake using high-resolution aeromagnetic and gravity data integrated with Differential Interferometric Synthetic Aperture Radar (DInSAR) analysis. Here we present the first results that provide insights into the tectonic framework of the earthquake. The ruptured fault trace delineated by DInSAR aligns with a distinct NW striking and NE dipping magnetic lineament within the Precambrian basement. The fault plane solution and numerical modeling indicate that the cause of the earthquake was 1.8 m displacement along a NW striking and NE dipping normal fault, rupturing at 21–24 km depth. We suggest that this seismic event was due to extensional reactivation of a crustal-scale Precambrian thrust splay within the Limpopo-Shashe orogenic belt.

**Plain Language Summary** Most earthquakes occur along plate boundaries. However, on 3 April 2017, a  $M_w$  6.5 earthquake rocked Moiyabana, Botswana, within the stable continental interior ~300 km away from the nearest zone of active tectonics. This earthquake occurred in a region where there is no surface expression of faults and where the last major tectonic event occurred ~2 Ga. We used high-resolution aeromagnetic and gravity data integrated with Differential Interferometric Synthetic Aperture Radar (DInSAR) analysis to investigate the fault that ruptured. We present the first results that show that the ruptured fault trace delineated by DInSAR aligns with a distinct NW striking and NE dipping magnetic lineament within the Precambrian basement. Our results further suggest that the cause of the earthquake was ~1.8 m displacement along a NW striking and NE dipping normal fault that ruptured at ~21–24 km depth. This seismic event was due to extensional reactivation of a crustal-scale Precambrian thrust splay within the Limpopo-Shashe orogenic belt that resulted from the collision of the Kaapvaal and Zimbabwe Cratons.

### 1. Introduction

On 3 April 2017 at 17:40:18 UTC, a  $M_w$  6.5 normal slip earthquake struck Moiyabana area of eastern Botswana (Figure 1a). The earthquake epicenter was determined to be at 22.678°S and 25.156°E, but its reported focal depth ranges from 23 km [GEOFON Earthquake Information Service, 2017] to 29 km [USGS Earthquake Catalogue, 2017]. The main shock was followed by a number of aftershocks clustered within 10 km of the epicentral area (Figure 1b). This event occurred at >300 km from the seismically active Okavango Rift Zone at a location within the Paleoproterozoic Limpopo-Shashe orogenic belt (Figure 1a), a geologic province with historically low seismic activity [e.g., Stamps et al., 2014]. This orogenic belt was formed due to collision between the Archean Kaapvaal and Zimbabwe Cratons and encloses a suture zone defined by crustal-scale thrusts [Roering et al., 1992]. The epicentral location and middle-lower crustal focal depth classify the earthquake as an intraplate seismic event.

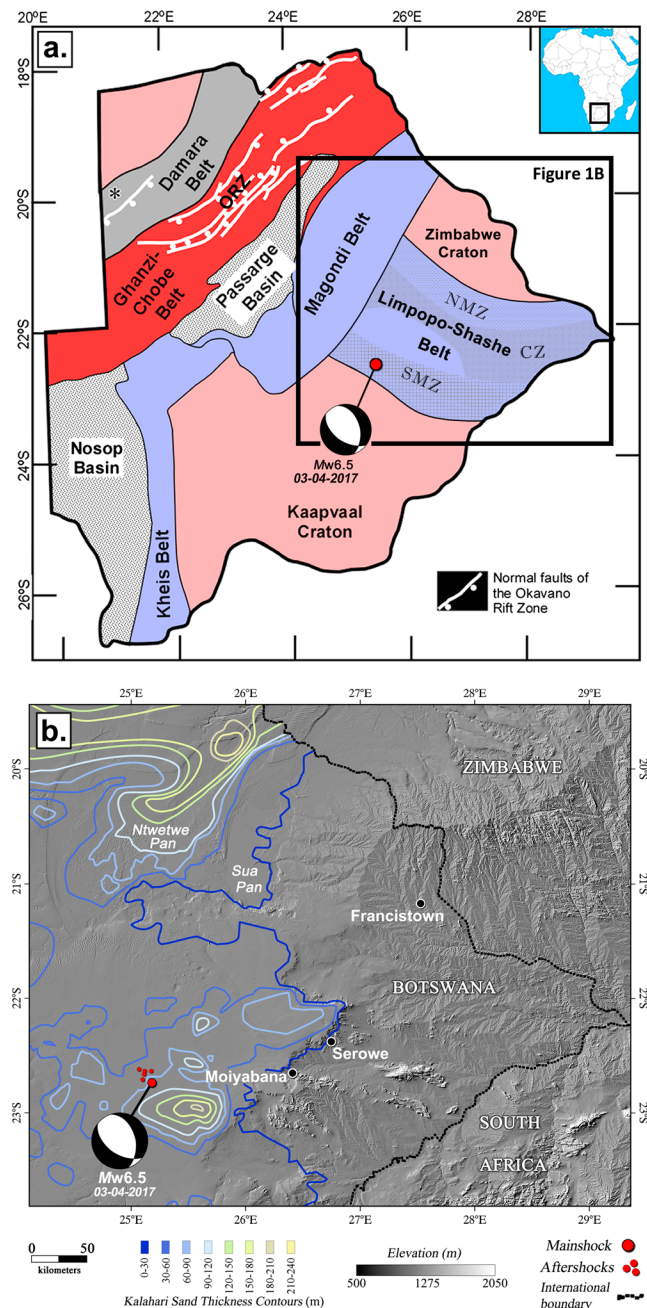


**Figure 1.** (a) Precambrian tectonic map of Botswana showing the spatial extent of Archean cratons, Proterozoic orogenic belts, earthquake epicenters, and focal plane mechanism solution of the  $M_w$  6.5 Moiyabana, Botswana, earthquake [from USGS Earthquake Catalogue, 2017a; GEOFON Earthquake Information Service, 2017a]. The geologic map is modified after Leseane et al. [2015] and Ranganai et al. [2002]. (b) Kalahari Sand thickness contour map (modified after Linol [2013]) draped on Shuttle Radar Topography Mission (SRTM) digital elevation model (DEM) of eastern Botswana. Pink dotted rectangle shows area covered in Figures 2 and 3.

Stable interior cratonic settings have been known to host numerous large-magnitude ( $M_w > 6.0$ ) earthquakes [Tuttle et al., 2002; Talwani, 2014]. Zoback [1992] and Nielsen et al. [2014] provide evidence for the importance of far-field stress exerted by plate boundary on the initiation of seismogenic intraplate deformation. Focusing of stress and triggering of intraplate earthquakes can also be initiated by flexural stresses that result from uncompensated lithospheric load [Assumpção and Sacek, 2013]. The relationship between preexisting basement features (such as faults and lithologic contacts) and intraplate seismicity [e.g., Kato et al., 2009; Shah et al., 2014] and the role of fluids as weakening agents in facilitating intraplate earthquakes [Kato et al., 2009; Rastogi et al., 2014; Pavan Kumar et al., 2017] have been documented.

Due to thick Kalahari Sand cover at the epicentral region of the Moiyabana, Botswana, earthquake (Figure 1b), there are no surface exposures of Precambrian rocks and there are no reports yet of surface ruptures associated with the earthquake. To provide a tectonic framework for this earthquake, we investigate the Precambrian basement structures using high-resolution aeromagnetic and ground gravity data and compare the fault geometry with earthquake rupture kinematics inferred from Differential Interferometric Synthetic Aperture Radar (DInSAR) and fault plane solutions. We build on the initial interpretation of the Precambrian basement structures carried out by Ranganai et al. [2002]. The availability of high-resolution potential field geophysical data over Botswana allows us to reinterpret and better delineate crustal-scale structures associated with the Limpopo-Shashe orogenic belt and its boundaries with the Zimbabwe and Kaapvaal Cratons.

### 1.1. Geological Background

The epicentral area of the 2017 Moiyabana earthquake is ~150 km west of Moiyabana, Botswana, located within the southwestern part of the Limpopo-Shashe orogenic belt (Figure 1a). This Paleoproterozoic orogenic belt encloses a lithospheric-scale suture zone that resulted from the collision between the Archean Zimbabwe Craton in the northeast and the Kaapvaal Craton to the southwest [Ranganai *et al.*, 2002]. Based on lithological and structural characteristics, the orogenic belt is divided into the Northern Marginal Zone (NMZ), the Central Zone (CZ), and the Southern Marginal Zone (SMZ) [Figure 1a; McCourt and Vearncombe, 1992; Ranganai *et al.*, 2002]. The Moiyabana earthquake epicenter is located near the southwestern boundary of the SMZ where the orogenic belt overlies the Kaapvaal Craton [Ranganai *et al.*, 2002]. The basement rocks of the SMZ are composed of Paleoproterozoic tonalite-trondhjemite-granite suite and granulites, deformed by NW striking pop-up constrictional tectonic structures with oppositely verging thrusts, folds, and shear zones [Ranganai *et al.*, 2002]. Multiple post-Paleoproterozoic tectonic episodes in eastern Botswana led to the formation of the NE striking Magondi orogenic belt which truncates the western part of the Limpopo orogenic belt, as well as the emplacement of the Precambrian-Mesozoic Okavango Dike Swarm (Figures S1a–S1d).

Previously published maps for tectonic terrane boundaries in eastern Botswana show the western part of the Limpopo-Shashe orogenic belt to be dominated by the Dinokwe Thrust (DT), Lechana Fault (LeF), Mahalapye Shear Zone (MsZ), Sunny Side Shear Zone (SsZ), and the Shashe Shear Zone (SSZ) (Figures S2a–S2d) [Ranganai *et al.*, 2002]. The epicenter of the 2017 Moiyabana earthquake is located within a crustal block that is bound to the northeast and southwest by the SW verging MsZ and DT, respectively.

## 2. Data and Methods

### 2.1. DInSAR

In order to isolate the coseismic surface deformation induced by the Moiyabana earthquake, we analyzed C band Synthetic Aperture Radar data acquired by the European Space Agency (ESA). The data span from 30 March to 11 April 2017, thus allowing us to capture the deformation from the 3 April earthquake. We obtained the data from relative orbit 14. The data were acquired in ascending pass with an incidence angle of 41° in the epicentral area and 13° satellite heading. The satellite to Earth line-of-sight (LOS) vector is 0.6011, 0.1331, and 0.7880 (ENU convention). The interferogram was computed according to the methodology described in Grandin [2015]. We used the Shuttle Radar Topography Mission (SRTM) digital elevation model (DEM) to subtract the topographic component. The phase was filtered using the Goldstein and Werner [1998] method and subsequently unwrapped using the branch-cut algorithm [Goldstein *et al.*, 1988].

### 2.2. Fault Geometry Model

To assess the fault plane geometry of the Moiyabana earthquake, we develop 25 models to test finite fault geometries in a three-dimensional single-layer elastic half-space [Lin and Stein, 2004] guided by the U.S. Geological Survey (USGS) focal plane solution for the main shock [Dziewonski *et al.*, 1981; Ekström *et al.*, 2012], the GEOFON focal plane solution for a  $M_w$  4.7 aftershock, and total seismic moments, respectively. We maintain the fault strike for each focal plane solution modeled but vary the dip incrementally by 5° for the main seismic event. The fault geometries are discretized with 5 km × 5 km patches vertically and horizontally. Assuming a range of isotropic elastic parameters (Poisson's ratio of 0.1–0.4 and Young's modulus of 60–100 GPa), we test applying fault slip on patches between 9 and 36 km deep along the fault geometries to calculate surface deformation [Okada, 1992] and total seismic moment such that we can relate results with the available, independent DInSAR data and moment magnitude estimates provided by the USGS and GEOFON. We provide more details of our fault geometry modeling in the supporting information (Text S1).

### 2.3. Aeromagnetic and Airborne Gravity Data

The Bouguer gravity anomaly and aeromagnetic data used in this study were provided by the Botswana Geoscience Institute. We provide detailed information on the gravity and aeromagnetic data used in this study in Text S1 and Tables S1 and S2. We applied mathematical filters to the gridded Bouguer gravity anomaly and aeromagnetic maps in order to enhance field gradients associated with Precambrian basement structures. We filtered and interpreted the gravity map in order to delineate regional-scale Precambrian terrane boundaries and interpreted filtered aeromagnetic maps to better delineate the crustal-scale basement

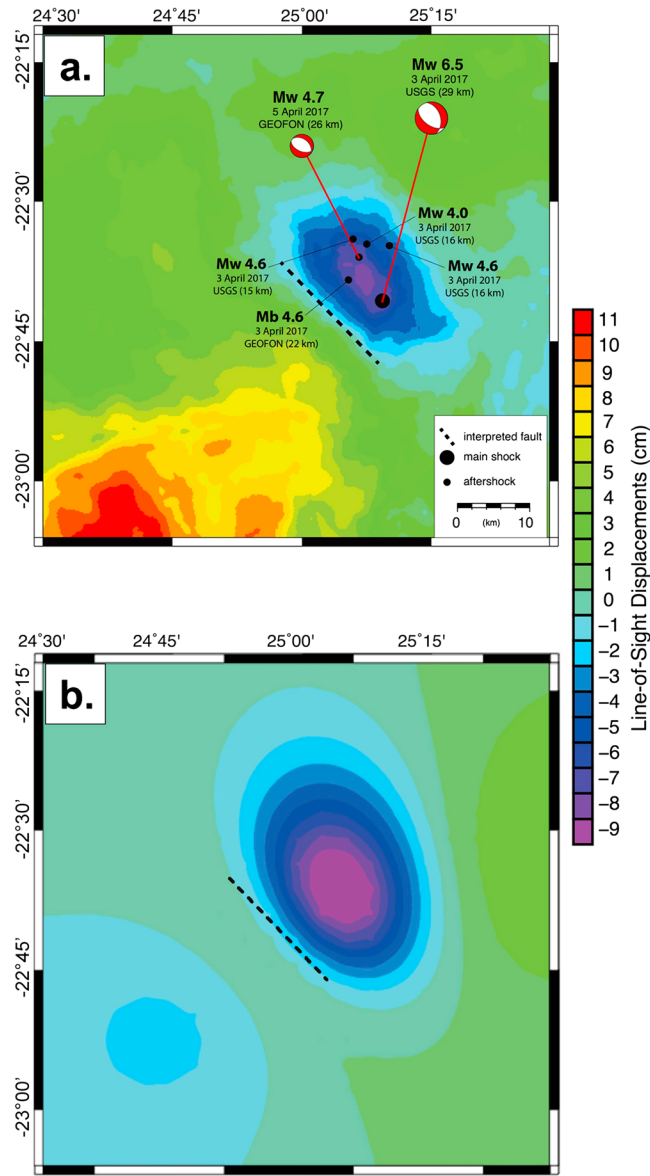


**Figure 2.** (a) Line-of-sight surface displacements from the unwrapped interferogram. Dashed line represents modeled fault trace projected along dip. Larger black circle is the epicenter of the  $M_w$  6.5 event and the smaller circles for the aftershocks. The focal mechanisms are from the USGS and GEOFON databases for each event as annotated. (b) Line-of-sight surface displacements from our preferred fault geometry model of the  $M_w$  6.5 event.

line-of-sight (LOS) displacement ( $\sim 8$  cm maximum) induced by subsidence to the northeast of the discontinuity (around the epicenter) and uplift to the southwest of the discontinuity.

### 3.2. Fault Geometry Model

We find that 1.8 m of slip occurred at 21–24 km depth on a NW-SE striking normal fault that dips  $53^\circ$  to the NE for the main shock event. Our preferred fault geometry for the main shock is consistent with nodal plane 1 of the USGS solution for the main event, of which we use the  $-114^\circ$  rake to impose that the slip and the modeled seismic moment is consistent with the moment magnitude of the event. The spatial pattern of vertical displacements at the surface correlates with the unwrapped DInSAR interferogram (Figures 2a and S4). Our results for the main shock suggest up to 9 cm of subsidence and/or down-drop of a fault block that occurs

structures within the epicentral region. Within the filtered aeromagnetic maps, we classify anomalies into low-frequency, long-wavelength ( $>4$  km) and high-frequency, short-wavelength ( $<1$ – $2$  km) lineaments. To delineate the possible downdip subsurface geometries of target long-wavelength, low-frequency magnetic anomalies within the Limpopo-Shashe orogenic belt, we evaluated the lateral and vertical variation in magnetic susceptibilities of crustal materials by utilizing the MAG3D inversion software for a three-dimensional (3-D) inversion of the aeromagnetic data (Figure S3). The MAG3D software was developed on the algorithm of *Li and Oldenburg* [1996]. We provide the details of aeromagnetic and gravity data used, filtering algorithms, and 3-D inversion applied to the aeromagnetic data in Text S1.

## 3. Results

### 3.1. DInSAR

In the unwrapped coseismic interferogram, we observe two areas of significant coseismic LOS motion within 20 km of the epicentral area (Figure 2a). This deformation takes the form of a distinct NW striking lobe within which the epicenter is located, bounded on the southwest by a sharp 18.5 km long,  $134^\circ$  striking discontinuity that separates it from another lobe. The location of the fringes, to the southwest of the epicenter, is consistent with an average of  $<5$  cm

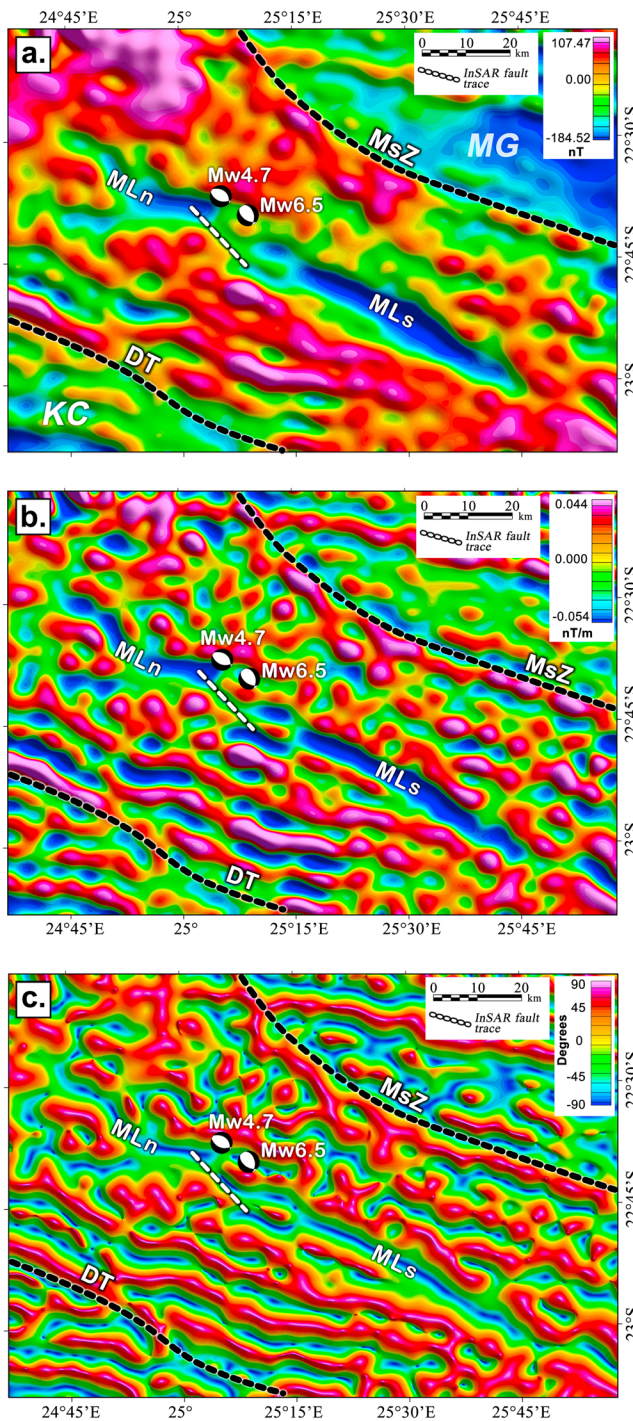


**Figure 3.** (a) The 6 km low-pass-filtered aeromagnetic map of the epicentral area. (b) First vertical derivative of the 6 km low-pass-filtered aeromagnetic map of the epicentral area. (c) Tilt angle derivative of the 6 km low-pass-filtered aeromagnetic map of the epicentral area. DT = Dinokwe Thrust; MG = Mahalapye Granite; MsZ = Mahalapye Shear Zone; MLn = northern segment of Moiyabana Lineament (ML); MLS = southern segment of Moiyabana Lineament (ML).

Swarms. The suppression of shallow anomalies in the upward continued magnetic data reveals a distinct  $>150$  km long,  $117^\circ$  striking magnetic low lineament (herein referred to as the Moiyabana Lineament)

to the east of the fault with  $\leq 1$  cm of minor uplift west of the fault. We use the GEOFON focal plane solution (strike =  $113^\circ$ , dip =  $51^\circ$ , rake =  $-100^\circ$ , and depth = 26 km) to constrain the aftershock geometry. The depth of the aftershock modeled here is likely imprecise because of poor instrumental coverage in the region; therefore, we emphasize that the  $M_w$  4.7 aftershock occurred NW of the main shock with slip an order of magnitude less than the main event. Consequently, predicted surface displacements are below the detection threshold of DInSAR.

### 3.3. Filtered Aeromagnetic and Gravity Anomaly Maps

From the first-order vertical derivative and tilt angle derivative of the Bouguer gravity anomaly and aeromagnetic maps (Figures S2a to S2d), regional interpretation of Precambrian terrane boundaries and their associated structures show that the earthquake epicenter is located along the contact of a NW striking gravity anomaly high (dotted black line in Figure S2b), midway between the DT and the MsZ (Figure S2d). The total magnetic intensity (TMI) and vertical derivative of the TMI of the epicentral area show the dominance of E-W to WNW striking high-frequency, short-wavelength magnetic lineaments (Figures S1a and S1b). However, 1 km upward continuation of the aeromagnetic data and the vertical derivative of the upward continued map reveal prominent NW striking longer-wavelength, lower frequency anomalies. These long-wavelength ( $>4$  km) anomalies correspond to older, Precambrian fabric [Ranganai et al., 2002] that are obscured and overprinted in the unfiltered aeromagnetic by the high-frequency, shorter-wavelength ( $<1-2$  km) anomalies associated with shallower and younger Okavango Dike

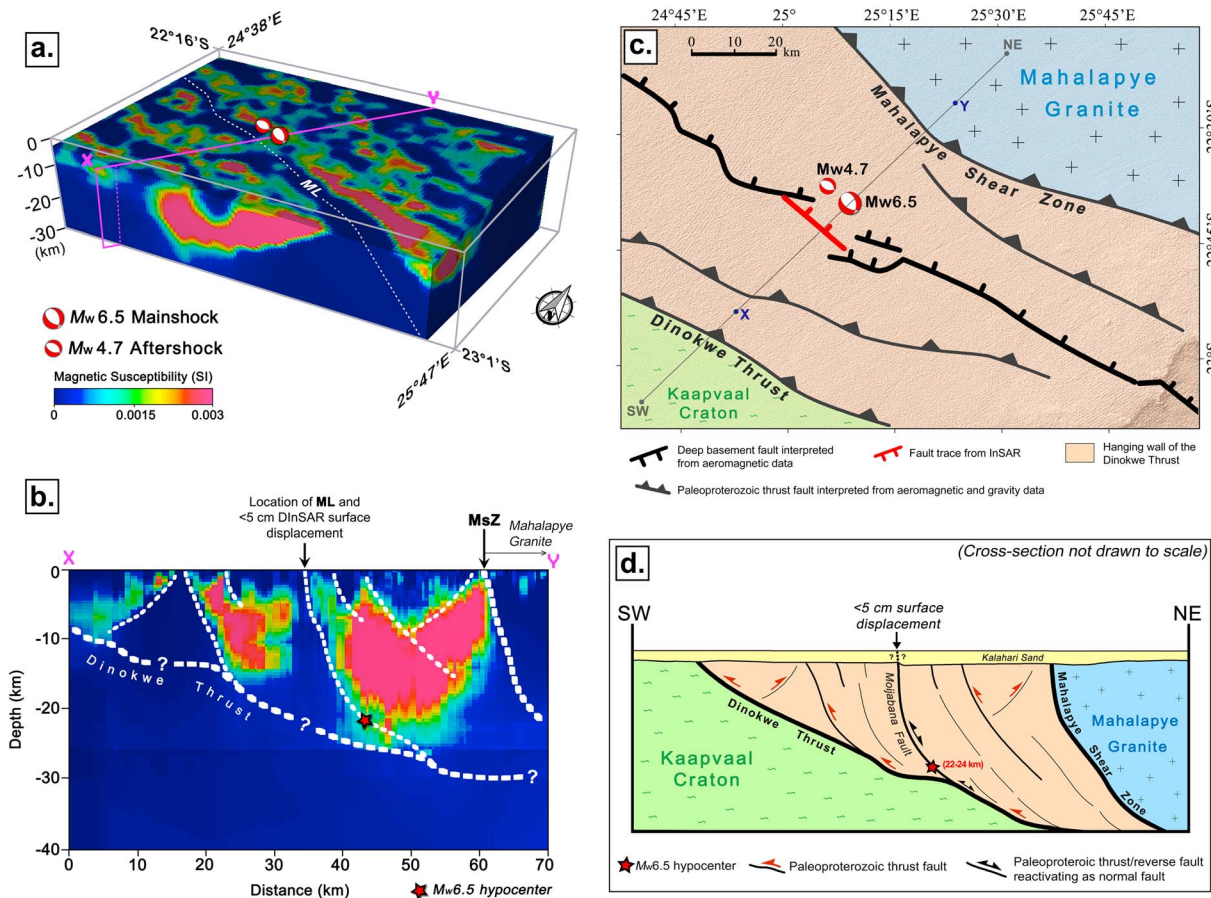


**Figure 4.** (a) Block covering the area in Figure 3, showing the three-dimensional (3-D) inversion of the aeromagnetic data. (b) Depth slice along transect X-Y (see Figure 4a) showing the variation in Curie point depth across the epicentral area. White dotted lines represent interpretation of tectonic terrain boundaries and their associated structures. (c) Interpretation of geotectonic setting of the 2017 Moiyabana earthquake based on DInSAR, aeromagnetic, and gravity data. (d) Conceptual two-dimensional (2-D) cross section across Figure 4c based on interpretations from Figures 3 and 4b.

\sim 7 km wide) to the magnetic data (Figure 3a). The vertical and tilt angle derivatives of the resultant low-pass-filtered magnetic map (Figures 3b and 3c) clearly delineate the along-strike continuation of the magnetic lineament and show that the lineament coincides with the line-of-sight displacement delineated by the DInSAR analyses (Figures 2a and 2b). The Moiyabana Lineament (ML) is segmented along strike, and we refer to these segments as MLn and MLs (Figures 3a–3c).

#### 3.4. Three-Dimensional Inversion of Aeromagnetic Data

On the 3-D inversion of the aeromagnetic data covering the epicentral area (Figure 4a), we observe variation in the vertical and lateral distribution of magnetic susceptibilities in the subsurface. The inversion shows that the Curie point depth (CPD) in the area, i.e., depth to the base of the magnetized crust is  $<30$  km, and generally decreases from northeast ( $\sim 25$  km) to southwest ( $\sim 10$  km; Figure 4b). The variations in magnetic susceptibilities reveal highly magnetized crustal blocks (0.0015–0.003 SI) that are truncated at depth by NE dipping regional discontinuities of very low magnetic susceptibilities ( $<0.00075$  SI). We clearly observe that a steep NE dipping discontinuity in the subsurface coincides with the ML (Figure 4b).

## 4. Discussion

### 4.1. Earthquake Epicentral Location in the Regional Geotectonic Setting

Ranganai *et al.* [2002] define the large-scale Neoarchean terrane boundaries within the western domain of the Paleoproterozoic Limpopo-Shashe orogenic belt. On the filtered aeromagnetic maps, post-

Paleoproterozoic dike swarms cutting across the older structures are represented by the high-frequency, short-wavelength lineaments (e.g., lineaments labeled "ODS" in Figures S2b–S2d and "D" in Figures S1a and S1b). The suppression of the high-frequency lineaments within the magnetic data reveals magnetic lineaments that are representative of the Neoarchean tectonic terrain boundaries and their associated structures (Figures 3a–3c and S1c). These terrain boundaries are interpretable from both aeromagnetic and gravity maps (Figures S2a–S2d) and are consistent with the results of previous regional-scale studies [Ranganai *et al.*, 2002]. Our results show that the epicenter of the 2017  $M_w$  6.5 Moiyabana earthquake is located within a NW striking crustal block bounded by the MsZ on the northeast and DT to the southwest (Figures 2b and 2d). Ranganai *et al.* [2002] showed that the DT and MsZ are Paleoproterozoic thrusts that were emplaced during the collision between the Zimbabwe Craton and the Kaapvaal Craton. The 3-D inversion of the aeromagnetic data provides a possible interpretation consistent with available data, which suggests a southwest vergence for the DT and MsZ (Figure 4b).

#### 4.2. Relationship Between Coseismic Surface Displacement and Magnetic Lineaments

The 134° striking coseismic discontinuity and associated average of <5 cm LOS subsidence (Figure 2a) interpreted from the unwrapped interferogram require ~1.8 m of dip slip (at 21–24 km depth) on a NW striking and NE dipping normal fault. The trace of this fault is located 7 km southwest of the earthquake epicenter. The proximity of the fault trace to the earthquake epicenter and the deep source of the  $M_w$  6.5 earthquake (and the occurrence of a  $M_w$  4.7 aftershock in a similar depth range) suggest a steeply dipping (72°–74°) fault plane. The relatively low dip angle (53°) of the nodal plane of the ruptured fault at depth thus suggests rupture on the downdip segment of a possible listric fault. On our filtered high-resolution aeromagnetic maps (Figures 3a–3c), we observe that the fault trace delineated from modeling the coseismic interferogram is subparallel to and links two segments of the ML (MLn and MLs). The result of our aeromagnetic data inversion is permissible to show that a listric geometry exists along the downdip segment of the ML (Figure 4b). Based on the trend (Figures 3a–3c) and interpreted dip (Figure 4b) of the ML, we interpret that the ML is a NE dipping structure, located within the hanging wall and is a thrust splay of the DT emplaced during the Paleoproterozoic collision between the Zimbabwe and Kaapvaal Cratons. Figure 4b shows the interpreted subsurface listric geometry of the ML structure. Here onward, we refer to the fault splay delineated by ML as the Moiyabana Fault (MF) (Figures 4a and 4b).

The possible listric geometry of the causative fault of the 2017  $M_w$  6.5 Moiyabana earthquake and the coincidence of the modeled fault geometry inferred from the DInSAR analysis with the MF (Figure 4c) suggest that the earthquake event is associated with the reactivation of the Precambrian thrust/reverse fault into a normal fault (Figure 4d). The focal plane mechanism solution of the main shock and resolved  $M_w$  4.7 aftershock show that the strike of the causative faults changes from NW-SE to WNW-ESE northward. Furthermore, the following sequence of low-magnitude aftershocks occurs at shallow depths as the rupture sequence evolves (see Figure 2a), also suggesting reactivation of an existing structure. The change in strike of nodal planes is consistent with the along-strike geometry of the MF directly southwest of the earthquake epicenters (Figures 2a, 2b, 3a, and 3c). Extensional reactivation of thrust faults and their associated seismicity have been previously documented. For example, the development of the Newark Basin border fault, Pennsylvania, was controlled by extensional reactivation of Paleozoic imbricate thrust faults [Ratcliffe *et al.*, 1986]. West [1993] observed seismogenic extensional reactivation of Paleocene thrust faults in north central Utah and southwestern Wyoming and suggested that the ramp-to-flat transition zones and leading edges along thrust faults are favorable for extensional reactivation. Using analogue modeling, Faccenna *et al.* [1995] showed that extensional reactivation of thrusts faults can occur in brittle material when the dip of the thrust fault exceeds 41°. Mohapatra and Johnson [1998] investigated the extensional reactivation of the Cretaceous Willard Thrust in the Great Salt Lake Basin, Utah, demonstrating that extensional slip on preexisting thrust ramps controlled the downdip listric geometry of the Tertiary normal faults.

We observe that the magnetic low signature of the MF varies from the magnetic expression of other lineaments of similar trend within the hanging wall of the DT (represented as magnetic highs; e.g., Figures 3a and S1c). Mosley [2010] characterized basement-rooted normal faults in the Okavanga Rift Zone by integrating aeromagnetic and magnetotelluric data and showed that basement faults that serve as conduits for fluid flow may be associated with magnetic low signatures. Weathering processes within fault zones due to fluid alteration and leaching away of iron could result in a magnetic low anomaly associated with these faults.

Therefore, we infer that the MF is a linear weathered zone within the crust, and we suggest that the MF possibly serves as a conduit for fluid flow within the crust. This hypothesis is supported by the observation of West [1993] that increased fluid pressures can further reduce effective stress and coefficient of friction across a low-angle fault plane thus allowing for the reactivation of such faults. Although the epicenter plots on a NW striking boundary between gravity high and low anomalies (Figure S2a; dotted black line in Figure S2b), the low resolution of the gravity data (Table S1) may be inadequate to resolve the low-density anomaly that is characteristic of weathered fault zones. Based on the location of the interferometric synthetic aperture radar fault trace (southwestern edge of ML; Figure 3), we also suggest that the MF is possibly a fault representing the contact between materials [Allam *et al.*, 2014] of high and low magnetization in the Precambrian crust.

The CPD beneath the  $M_w$  6.5 earthquake epicenter is deepest in the area (~25 km). The depth to the base of the magnetized crust is directly related to the Curie point (550–580°C), being the typical range of temperatures at which magnetic minerals lose their ferromagnetism [Arnaiz-Rodrigues and Orihuela, 2013]. The brittle-ductile (BD) transition zone within the Earth's crust is typically 250–400°C [Scholz, 1988]. The depths of the Moiyabana earthquake hypocenter (21–24 km) and the local CPD suggest that the seismic faulting possibly took place within the middle-lower crust (assuming crustal depth estimates for the SMZ from Nguuri *et al.* [2001]), at a level that is deeper than the brittle-ductile transition (BD) zone. Pavan Kumar *et al.* [2017] investigated the relationship between electrically conductive fault zones and lower crustal intraplate seismicity and clearly demonstrated that fluidized crustal-scale faults are prone to seismogenic fault slips. Seismogenic slip along fault zones at lower crustal depths can be induced by elevated fluid pressures and decrease in the mechanical strength of the entire host rock.

#### 4.3. Source of Stresses

The tectonic implications of the Moiyabana earthquake depend on whether it reflects the influence of far-field stresses that are driving present-day rifting in segments of the East African Rift System (EARS) or regional mantle-related dynamics or both. Rifting in the Okavango Rift Zone (nearest segment of the EARS) is defined by NE striking normal faults acted upon by NW-SE directed tensional forces from lithospheric buoyancy [Ghosh *et al.*, 2008; Stamps *et al.*, 2010, 2014], but the orientation of tensional stress required for the Moiyabana earthquake is different (i.e., northeast directed). However, the focal mechanism of the Moiyabana earthquake is consistent with the local stress regime predicted by Bird *et al.* [2006].

Bird *et al.* [2006] showed that previously reported dominant NW-SE directed maximum compressive horizontal stresses south of latitude 20°S (the Wegener stress anomaly [e.g., Andreoli *et al.*, 1996; Viola *et al.*, 2005]) are caused by a NE-SW extensional tectonic stress enhanced by proximity to the Somalia-Nubia Euler pole. Bird *et al.* [2006] further suggested that the NW-SE extension associated with the Okavango Rift Zone is a result of stress interactions of unbroken lithosphere around the southward propagating tip of the East African Rift. Yu *et al.* [2015] observed dominant NE-SW fast orientations of shear wave splitting times, interpreted to be associated with mantle anisotropy beneath the Okavango Rift Zone, the Limpopo-Shashe orogenic belt, the Kaapvaal Craton, and the Zimbabwe Craton. Yu *et al.* [2015] suggest that the source of this mantle anisotropy is a NE directed differential basal drag of cratonic blocks, which is an interpretation consistent with previous studies of seismic anisotropy [i.e., Fouch and Rondenay, 2006; Bagley and Nyblade, 2013], or fossil anisotropy in the keel [Silver *et al.*, 2004]. We consider that at the focal depth of the 2017  $M_w$  6.5 Moiyabana earthquake, the crust is almost certainly in a triaxial state of compression. Therefore, we suggest that both the Wegener stress anomaly model and variation in cratonic basal drag velocities beneath the Limpopo-Shashe orogenic belt may provide some insight into the source of the normal fault stress state (in which  $\sigma_1$  is vertical and is greater than NE-SW directed  $\sigma_3$ ) around the earthquake epicentral region. Although the sources of stress for intraplate seismicity have been mostly attributed to far-field tectonics and uncompensated lithospheric load [Zoback, 1992; Assumpção and Sacek, 2013; Nielsen *et al.*, 2014], we hereby highlight the possible role of mantle anisotropy in the generation of large-magnitude ( $M_w > 6.0$ ) earthquakes within stable interior cratonic settings.

#### 5. Conclusions

The integration of DInSAR, aeromagnetic, and gravity data allows us to rapidly probe the causative fault of the 2017  $M_w$  6.5 Moiyabana, Botswana, earthquake. We present the first results of investigation on the earthquake and provide insight into the geotectonic setting of its causative fault. Our study shows that the 21–24 km deep seismic event is an example of intraplate seismicity and is associated with the

extensional reactivation of a Neoproterozoic thrust splay, named the Moiyabana Fault. We suggest that there is a need to better understand the rupture dynamics at the focal depth of the earthquake, the source of normal fault stresses, and the implications for intraplate seismicity.

### Acknowledgments

This work was partially supported by the National Science Foundation (NSF) grant EAR10-09988 to E.A. Atekwana. We thank the Botswana Geoscience Institute (BGI) of the Government of Botswana for releasing the aeromagnetic and gravity data used for this study. We also acknowledge the support of the Botswana International University of Science and Technology (BIUST) as the data were released as part of the BIUST-BGI collaboration. The aeromagnetic data can be obtained from the GeoPRISMS data portal (DOI: 10.1594/EDAA/324147). The Sentinel-1 SAR data are available from the European Space Agency (ESA). Processing of Sentinel-1 was performed on the S-CAPAD platform, IPGP, France. Seismic data utilized in this work can be found at the Incorporated Research Institutes for Seismology (IRIS) data management center ([breq\\_fast@iris.washington.edu](mailto:breq_fast@iris.washington.edu)) and GEOFON Program, GFZ, Potsdam ([breq\\_fast@gfz-potsdam.de](mailto:breq_fast@gfz-potsdam.de)). We thank Susan Webb and an anonymous reviewer for their detailed and constructive reviews. This is the Oklahoma State University Boone Pickens School of Geology contribution 2017-73.

### References

- Allam, A. A., Y. Ben-Zion, and Z. Peng (2014), Seismic imaging of a bimaterial interface along the Hayward fault, CA, with fault zone head waves and direct  $P$  arrivals, *Pure Appl. Geophys.*, 171(1), 2993–3011.
- Andreoli, M. A. G., M. Doucoure, J. Van Bever Donker, D. Brandt, and N. J. B. Andersen (1996), Neotectonics of southern Africa: A review, *Afr. Geosci. Rev.*, 3(1), 1–16.
- Arkani-Hamed, J. (1988), Differential reduction-to-the-pole of regional magnetic anomalies, *Geophysics*, 53, 1592–1600.
- Arnaiz-Rodrigues, M. S., and N. Orihuela (2013), Curie point depth in Venezuela and the Eastern Caribbean, *Tectonophysics*, 590, 38–51.
- Assumpção, M., and V. Sacek (2013), Intra-plate seismicity and flexural stresses in central Brazil, *Geophys. Res. Lett.*, 40, 487–491, doi:10.1002/grl.50142.
- Bagley, B., and A. A. Nyblade (2013), Seismic anisotropy in eastern Africa, mantle flow, and the African superplume, *Geophys. Res. Lett.*, 40, 1500–1505, doi:10.1002/grl.50315.
- Baranov, V. (1957), A new method for interpretation of aeromagnetic maps: Pseudo-gravimetric anomalies, *Geophysics*, 22, 359–383.
- Bird, P., Z. Ben-Avraham, G. Schubert, M. Andreoli, and G. Viola (2006), Patterns of stress and strain rate in southern Africa, *J. Geophys. Res.*, 111, B08402, doi:10.1029/2005JB003882.
- Blakely, R. J. (1995), *Potential Theory in Gravity and Magnetic Applications*, Cambridge Univ. Press, Cambridge.
- Briggs, I. C. (1974), Machine contouring using minimum curvature, *Geophysics*, 39(1), 39–48.
- Dziewonski, A. M., T. A. Chou, and J. H. Woodhouse (1981), Determination of earthquake source parameters from waveform data for studies of global and regional seismicity, *J. Geophys. Res.*, 86, 2825–2852, doi:10.1029/JB086iB04p02825.
- Ekström, G., M. Nettles, and A. M. Dziewonski (2012), The global CMT project 2004–2010: Centroid-moment tensors for 13,017 earthquakes, *Phys. Earth Planet. Inter.*, 200–201, 1–9, doi:10.1016/j.pepi.2012.04.002.
- Faccenna, C., T. Nalpas, J. P. Brun, P. Davy, and V. Bosi (1995), The influence of pre-existing thrust faults on normal fault geometry in nature and in experiments, *J. Struct. Geol.*, 17, 1139–1149.
- Fouch, M. J., and S. Rondenay (2006), Seismic anisotropy beneath stable continental interiors, *Phys. Earth Planet. Int.*, 158(2), 292–320.
- GEOFON Earthquake Information Service (2017), GEOFON earthquake catalogue. [Available at <http://geofon.gfz-potsdam.de/eqinfo/eqinfo.php>, accessed 23 May 2017.]
- Goldstein, R. M., and C. L. Werner (1998), Radar interferogram filtering for geophysical applications, *Geophys. Res. Lett.*, 25(21), 4035–4038, doi:10.1029/1998GL900033.
- Goldstein, R. M., H. A. Zebker, and C. L. Werner (1988), Satellite radar interferometry: Two-dimensional phase unwrapping, *Radio Sci.*, 23(4), 713–720, doi:10.1029/RS023i004p00713.
- Grandin, R. (2015), Interferometric processing of SLC Sentinel-1 TOPS data, Proc. of the 2015 ESA Fringe Workshop, ESA Special Publication, 731 pp.
- Ghosh, A., W. E. Holt, L. Wen, A. J. Haines, and L. M. Flesch (2008), Joint modeling of lithosphere and mantle dynamics elucidating lithosphere-mantle coupling, *Geophys. Res. Lett.*, 35, L16309, doi:10.1029/2008GL034365.
- Henderson, R. G., and I. Zietz (1949), The upward continuation of anomalies in total magnetic intensity fields, *Geophysics*, 14(4), 517–534.
- Jacobsen, B. H. (1987), A case for upward continuation as a standard separation filter for potential-field maps, *Geophysics*, 52, 1138–1148.
- Kato, A., E. Kurashimo, T. Igashiki, S. Sakai, T. Iidaka, M. Shinohara, T. Kanazawa, T. Yamada, N. Hirata, and T. Iwasaki (2009), Reactivation of ancient rift systems triggers devastating intraplate earthquakes, *Geophys. Res. Lett.*, 36, L05301, doi:10.1029/2008GL036450.
- Leseane, K., E. A. Atekwana, K. L. Mickus, M. G. Abdelsalam, E. M. Shemang, and E. A. Atekwana (2015), Thermal perturbations beneath the incipient Okavango Rift Zone, northwest Botswana, *J. Geophys. Res. Solid Earth*, 120, 1210–1228, doi:10.1002/2014JB011029.
- Li, Y., and D. W. Oldenburg (1996), 3-D inversion of magnetic data, *Geophysics*, 61, 394–408.
- Lin, J., and R. S. Stein (2004), Stress triggering in thrust and subduction earthquakes and stress interaction between the southern San Andreas and nearby thrust and strike-slip faults, *J. Geophys. Res.*, 109, B02303, doi:10.1029/2003JB002607.
- Linol, B. (2013), Sedimentology and sequence stratigraphy of the Congo and Kalahari basins of south Central Africa and their evolution during the formation and break-up of west Gondwana, PhD thesis, 375 pp., Nelson Mandela metropolitan Univ., Port Elizabeth, 19 March.
- McCourt, S., and J. R. Vearnscombe (1992), Shear zones of the Limpopo Belt and adjacent granitoid-greenstone terranes: Implications for late Archaean collision tectonics in southern Africa, *Precambrian Res.*, 55, 553–570.
- Miller, H. G., and V. Singh (1994), Semiquantitative techniques for the removal of directional trends from potential field data, *J. Appl. Geophys.*, 32, 199–211.
- Mohapatra, G. K., and R. A. Johnson (1998), Localization of listric faults at thrust fault ramps beneath the Great Salt Lake Basin, Utah: Evidence from seismic imaging and finite element modeling, *J. Geophys. Res.*, 103, 10,047–10,063, doi:10.1029/98JB00023.
- Mosley, K. S. (2010), Geophysical characterization of faults of the Okavango Rift Zone, Northwest Botswana, Africa, MS thesis, 93 pp., Oklahoma state Univ., Stillwater, 01 May.
- Nguuri, T. K., J. Gore, D. E. James, S. J. Webb, C. Wright, T. G. Zengeni, O. Gwava, and J. A. Snook (2001), Crustal structure beneath southern Africa and its implications for the formation and evolution of the Kaapvaal and Zimbabwe cratons, *Geophys. Res. Lett.*, 28(13), 2501–2504, doi:10.1029/2000GL012587.
- Nielsen, S. B., R. A. Stephenson, and C. Schiffer (2014), Deep controls on intraplate basin inversion, in *Intraplate Earthquakes*, pp. 257–274, Cambridge Univ. Press, Cambridge, U. K.
- Okada, Y. (1992), Internal deformation due to shear and tensile faults in a half-space, *Bull. Seismol. Soc. Am.*, 82(2), 1018–1040.
- Pavan Kumar, G., P. Mahesh, M. Nagar, E. Mahender, V. Kumar, K. Mohan, and M. Ravi Kumar (2017), Role of deep crustal fluids in the genesis of intraplate earthquakes in the Kachchh region, northwestern India, *Geophys. Res. Lett.*, 44, 4054–4063, doi:10.1002/2017GL072936.
- Ranganai, R. T., A. B. Kampunzu, E. A. Atekwana, B. K. Paya, J. G. King, D. I. Koosimile, and E. H. Stettler (2002), Gravity evidence for a larger Limpopo Belt in southern Africa and geodynamic implications, *Geophys. J. Int.*, 149(3), F9–F14.
- Rastogi, B. K., P. Mandal, and S. K. Biswas (2014), Seismogenesis of earthquakes occurring in the ancient rift basin of Kachchh, western India, in *Intraplate Earthquakes*, edited by P. Talwani, pp. 126–161, Cambridge Univ. Press, New York.

- Ratcliffe, N. M., W. C. Burton, R. M. D'angelo, and J. K. Costair (1986), Low-angle extensional faulting, reactivated mylonites, and seismic reflection geometry of the Newark basin margin in eastern Pennsylvania, *Geology*, 14, 766–770.
- Reeves, C. V., and D. G. Hutchins (1976), The national gravity survey of Botswana, 1972–73, Lobatse: Director, Geological Survey Department.
- Roering, C., D. D. Van Reenen, C. A. Smit, J. M. Barton, J. H. De Beer, M. J. De Wit, E. H. Stettler, J. F. Van Schalkwyk, G. Stevens, and S. Pretorius (1992), Tectonic model for the evolution of the Limpopo Belt, *Precambrian Res.*, 55(1–4), 539–552.
- Salem, A., S. Williams, J. D. Fairhead, R. Smith, and D. Ravat (2008), Interpretation of magnetic data using tilt-angle derivatives, *Geophysics*, 73, L1–L10.
- Scholz, C. H. (1988), The brittle-plastic transition and the depth of seismic faulting, *Geol. Rundsch.*, 77(1), 319–328.
- Shah, A. K., J. W. Horton, W. C. Burton, D. B. Spears, and A. K. Gilmer (2014), Subsurface geologic features of the 2011 central Virginia earthquakes revealed by airborne geophysics, *Geol. Soc. Am. Spec. Pap.*, 509, SPE509–17.
- Silver, P. G., M. J. Fouch, S. S. Gao, and M. Schmitz (2004), Seismic anisotropy, mantle fabric, and the magmatic evolution of Precambrian southern Africa, *S. Afr. J. Geol.*, 107(1–2), 45–58.
- Stamps, D. S., L. M. Flesch, and E. Calais (2010), Lithospheric buoyancy forces in Africa from a thin sheet approach, *Int. J. Earth Sci.*, 99(7), 1525–1533.
- Stamps, D. S., L. M. Flesch, E. Calais, and A. Ghosh (2014), Current kinematics and dynamics of Africa and the East African Rift System, *J. Geophys. Res. Solid Earth*, 119, 5161–5186, doi:10.1002/2013JB010717.
- Swain, C. J. (1976), A FORTRAN IV program for interpolating irregularly spaced data using the difference equations for minimum curvature, *Comput. Geosci.*, 1(4), 231–240.
- Talwani, P. (Ed.) (2014), *Intraplate Earthquakes*, p. 368, Cambridge Univ. Press, New York.
- Tuttle, M. P., E. S. Schweig, J. D. Sims, R. H. Lafferty, L. W. Wolf, and M. L. Haynes (2002), The earthquake potential of the New Madrid seismic zone, *Bull. Seismol. Soc. Am.*, 92, 2080–2089.
- USGS Earthquake Catalogue (2017), US Geological Survey earthquake catalogue. [Available at <https://earthquake.usgs.gov/earthquakes/>, accessed 23 May 2017.]
- Viola, G., M. Andreoli, Z. Ben-Avraham, I. Stengel, and M. Reshef (2005), Offshore mud volcanoes and onland faulting in southwestern Africa: Neotectonic implications and constraints on the regional stress field, *Earth Planet. Sci. Lett.*, 231, 147–160.
- West, M. W. (1993), Extensional reactivation of thrust faults accompanied by coseismic surface rupture, southwestern Wyoming and north-central Utah, *Geol. Soc. Am. Bull.*, 105, 1137–1150.
- Yu, Y., S. S. Gao, M. Moidaki, C. A. Reed, and K. H. Liu (2015), Seismic anisotropy beneath the incipient Okavango rift: Implications for rifting initiation, *Earth Planet. Sci. Lett.*, 430, 1–8.
- Zoback, M. L. (1992), First- and second-order patterns of stress in the lithosphere: The World Stress Map Project, *J. Geophys. Res.*, 97(B8), 11,703–11,728, doi:10.1029/92JB00132.